# Prediction of Columnar to Equiaxed Transition during Diffusion-Controlled Dendritic Alloy Solidification

C.Y. WANG and C. BECKERMANN

A model is presented to predict the columnar to equiaxed transition (CET) in alloy castings. The model is based on a multiphase approach and accounts for heat and solute diffusion, as well as for grain nucleation, growth, and morphology. The model equations are applicable to both columnar and equiaxed dendritic solidification, thus offering an efficient single-domain formulation. A fixed grid, fully implicit finite-difference procedure is employed in the numerical solution, and a novel front tracking technique is incorporated that is also implicit in nature and readily applies to multidimensional situations. Calculations are performed for one-dimensional (1-D) and two-dimensional (2-D) castings of Al-Cu and Sn-Pb alloys. The calculated CET positions are compared with previous measurements in a (1-D) ingot cast under well-controlled conditions, and good agreement is found. The effects of various casting parameters on the CET are numerically explored.

## I. INTRODUCTION

CASTINGS of metallic alloys may exhibit either wholly columnar or entirely equiaxed grain structures, depending on the alloy composition and the solidification conditions. Another more complex structure, which is often observed in chill castings, is composed of both kinds of grains. This mixed mode of solidification occurs if equiaxed grains can nucleate and grow in the bulk liquid ahead of the advancing columnar front, resulting in a transition from a columnar zone to a central equiaxed zone in some as-cast structures.[1,2,3]

The prediction of the columnar to equiaxed transition (CET) is of great interest for the evaluation and design of the mechanical properties of solidified products. To this aim, it is necessary to understand the CET mechanisms and to develop a model to quantify important features of the composite structure, such as the relative size of the two zones. As suggested by many previous studies, the CET, caused by the competition between columnar and equiaxed growth, is primarily governed by such casting parameters as the alloy composition, pouring superheat, nuclei density present in the melt, cooling capacity at the metal/mold interface, and melt convection. Qualitatively, it can be anticipated than the CET occurs earlier when an alloy has a higher solute level, lower pouring temperature, smaller thermal gradient, higher nuclei density present in the melt, and more vigorous melt convection. However, quantitative predictions of the CET require a more thorough understanding and a full account of all physical mechanisms involved. For small specimens of almost uniform temperature, experimental observations indicate that nucleation and growth of the equiaxed grains ahead of the columnar front are the most important mechanisms for causing the CET.[4] For sizable castings, the temperature field significantly affects the competitive columnar and equiaxed solidification, since columnar growth is constrained by the movement of the isotherms, and equiaxed growth ahead of the columnar front in turn alters the temperature field through the release of latent heat. The complications of these multiple mechanisms have hindered the mathematical modeling of the CET phenomenon.

Only recently have efforts been made to theoretically model the CET. Hunt[5] first developed an analytical model by considering steady-state columnar and equiaxed growth. The model qualitatively reveals the influences of alloy composition, nuclei density, and cooling rate on the CET. Subsequently, Flood and Hunt[6,7] extended the work to model dynamically the CET in a one-dimensional (1-D) ingot. They incorporated grain nucleation and growth principles into a heat-flow calculation, and simulated the CET as a Stefan-like discontinuity interface. Although their work significantly advances the prediction of the CET, it suffers from several limitations. First, solute is not conserved in their model, as noticed in a number of subsequent investigations.[8,9] This leads to erroneous predictions of the volume fraction of equiaxed grains whose growth is mainly controlled by constitutional undercooling and therefore makes it impossible to capture the CET accurately. Second, their model is a multidomain formulation in which different governing equations are applied to the columnar and equiaxed zones. The solution of such equations requires explicit tracking of the interface separating the two zones and the use of appropriate matching conditions between the two regions. It is well known that great difficulties are associated with the numerical implementation of such a model, in particular in multidimensional situations.

Other numerical studies of predicting the grain growth and CET adopt a completely different approach, namely, a probabilistic method based on the Monte-Carlo procedure. Notable work includes that by Brown and Spittle,[4] Zhu and Smith,[10] and Rappaz and Gandin.[11] Being capable of producing computed two-dimensional (2-D) microstructures that closely resemble those observed in real micrographic cross sections, these models, however, either lack a rigorous physical basis or invoke certain simplifications. For example, the physical mechanisms of nucleation and growth of dendritic grains have

C.Y. WANG, Graduate Student and Research Assistant, and C. BECKERMANN, Associate Professor, are with the Department of Mechanical Engineering, University of Iowa, Iowa City, IA 52242.

Manuscript submitted March 12, 1993.

not been properly accounted for in the statistical models by Brown and Spittle and Zhu and Smith. A uniform temperature field has been assumed, and solute diffusion has not been considered by Rappaz and Gandin.

Comprehensive experiments on the CET have been conducted by Weinberg and co-workers in laboratory ingots cooled from below for various Sn-Pb alloys[12] and an Al-3 wt pct Cu alloy.[13] The relationship between the casting parameters and the CET position has been established for these alloys. However, no systematic comparisons between these experiments and theory have been attempted so far.[14]

The present article describes a new approach to modeling the CET during dendritic solidification. The primary objective is to remove several of the limitations associated with previous models and, thus, to allow for quantitative predictions of the CET in alloy castings. Another goal of the present study is to perform comprehensive comparisons between theory and experiment, which represents a serious gap in the existing literature. As a first step, only heat and solute diffusion is considered, while melt convection and the transport of solid grains will be included in a future investigation. The mathematical formulation is based upon a multiphase model recently developed by the present authors.[15] The model distinguishes the interdendritic and extradendritic liquid as two different phases, by noting the fact that they are associated with two disparate interfacial length scales. A set of macroscopic equations governing solute diffusion is derived using the volume-averaging procedure. The final model equations account for nucleation and growth of dendritic grains, dendrite morphology, and the solute balance as well. The model has been applied to purely equiaxed and columnar solidification systems in which the temperature is almost uniform, and the predictions have been thoroughly validated through comparison with a wide range of experimental data available in the literature.[16] A salient feature of the multiphase model is that the conservation equations are, in principle, applicable to both columnar and equiaxed types of solidification, except for some supplementary relations (shown in Section II). Therefore, the present model, consisting of one set of equations throughout the system domain, is well suited for simulating mixed columnar and equiaxed solidification; matching conditions between different regions are unnecessary, and a fixed grid is allowed in numerical implementations. Coupled with the heat-flow equation, the model provides a complete methodology for CET simulations.

In the following sections the present multiphase model is first described, which is followed by numerical solution procedures. Numerical results are then obtained for an Al-3 wt pct Cu alloy in both 1-D and 2-D geometries. The effects of various physical parameters on the CET position are discussed. Finally, simulation results for Al-Cu and Sn-Pb alloys are compared with previous experimental data for the CET in 1-D castings.

## II. MATHEMATICAL MODEL

The system under investigation is shown in Figure 1 and consists, in the most simple case, of a 1-D casting

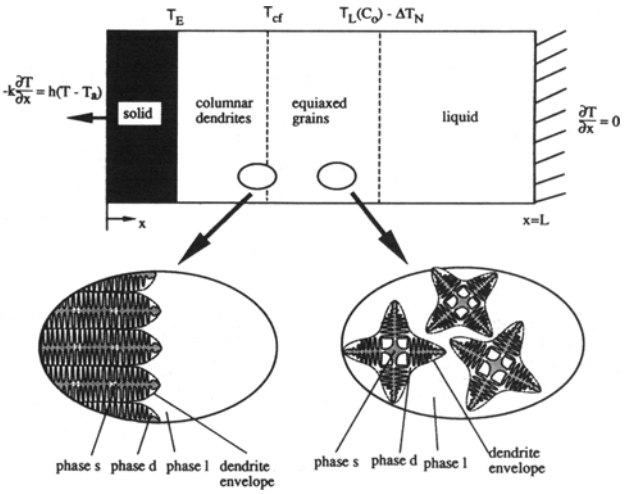


Fig. 1 — Schematic of the physical problem and illustration of the multiphase approach.

in which mixed columnar and equiaxed growth occurs. The equiaxed grains compete with the advancing columnar grains; when the equiaxed crystals are small, they are swallowed by the approaching columnar front and transformed into columnar dendrites. Conversely, if the undercooled zone ahead of the columnar front is relatively large and the density of crystals high, the equiaxed crystals may have enough time to reach a sufficiently high volume fraction to block the columnar crystal growth. The latter case results in the CET in the final microstructure of a solidified material. A criterion for the CET to occur was first proposed by Hunt[5] and later confirmed by Brown and Spittle.[4] That is, the equiaxed grain volume fraction ($\varepsilon_s + \varepsilon_d$) immediately ahead of the columnar front must exceed 0.49 to stop the columnar growth. The multiple region problem, as shown in Figure 1, is dealt with by a multiphase approach.[15] The model equations together with their assumptions are presented in the following subsection.

### A. *Model Equations*

In the multiphase approach proposed by Wang and Beckermann,[15] a control volume containing either columnar or equiaxed dendrites is considered to consist of three phases: the solid $s$, the interdendritic liquid $d$, and the extradendritic liquid $l$. This is schematically shown in Figure 1. The two liquid phases are associated with different interfacial length scales and possess different transport behaviors. A dendrite envelope is defined as the interface separating the interdendritic and extradendritic liquid phases, and its movement is governed by the growth model for dendrite tips. (Wang and Beckermann[15,16] provide a thorough discussion of this multiphase approach.)

The specific assumptions implied in the subsequent model equations are summarized as follows.

(1) Local thermal equilibrium exists between the liquid and solid phases, which can be justified by the large value of the Lewis number of metallic alloys.
(2) Melt convection and solid transport are neglected.

(3) The densities of the solid and liquid phases are constant and equal.
(4) The interdendritic liquid is solutally well mixed, whereas substantial undercooling is allowed in the extradendritic liquid for grain growth.
(5) The dendrite envelope is spherical, namely, $\phi_e = 1$. This has been shown in Reference 16 to be a good approximation for slightly nonspherical dendrite envelopes (*i.e.*, $0.8 \le \phi_e \le 1$).
(6) Macroscopic solute diffusion on the system scale is negligible.

Under the first two assumptions, a single heat conduction equation can be written for the mixture temperature:

$$c_p \frac{\partial T}{\partial t} = \nabla \cdot (k \nabla T) + \Delta h \frac{\partial \varepsilon_s}{\partial t} \qquad [1]$$

where $T$ and $\varepsilon_s$ stand for the temperature and solid volume fraction, respectively, $c_p$ and $\Delta h$ are the volumetric specific and latent heats, respectively, and $k$ denotes the effective thermal conductivity of the solid-liquid mixture, which is evaluated as the volume fraction weighted mean of the solid and liquid thermal conductivities and can, in principle, be anisotropic. The solid fraction evolution that appears in the last term of Eq. [1] is determined from the following solute diffusion model for the present three-phase system.

*Envelope motion (dendrite tip growth)*

$$\frac{\partial}{\partial t}(\varepsilon_s + \varepsilon_d) = S_e \bar{w}_{ne} = \frac{S_e D_l m_l (\kappa - 1) \bar{C}_e}{\pi^2 \Gamma} [\mathrm{Iv}^{-1}(\Omega)]^2 \qquad [2]$$

*Solute balance of phase s*

$$\frac{\partial (\varepsilon_s \langle C_s \rangle^s)}{\partial t} = \bar{C}_{sd} \frac{\partial \varepsilon_s}{\partial t} + \frac{S_s D_s}{\ell_{sd}} (\bar{C}_{sd} - \langle C_s \rangle^s) \qquad [3]$$

*Solute balance of phase d*

$$\varepsilon_d \frac{\partial \bar{C}_e}{\partial t} + (\kappa - 1) \bar{C}_e \frac{\partial \varepsilon_s}{\partial t} = -\frac{S_e D_l}{\ell_d} (\bar{C}_e - \langle C_l \rangle^l) - \frac{S_s D_s}{\ell_{sd}} (\bar{C}_{sd} - \langle C_s \rangle^s) \qquad [4]$$

*Solute balance of phase $\ell$*

$$\frac{\partial [\varepsilon_l \langle C_l \rangle^l]}{\partial t} = \bar{C}_e \frac{\partial \varepsilon_l}{\partial t} + \frac{S_e D_l}{\ell_{ld}} (\bar{C}_e - \langle C_l \rangle^l) \qquad [5]$$

This set of equations has been rigorously derived by the volume-averaging technique.[15] Apart from the physical properties that are explained in the Nomenclature, several notations are clarified here. First, the term $\langle C_k \rangle^k$ denotes the volume-averaged intrinsic concentration of a phase $k$, with $\langle \cdot \rangle$ being the conventional symbol used in the volume-averaging method. Physically, the term $\langle C_k \rangle^k$ is nothing more than the mean concentration in a phase. The symbol $\bar{C}_e$ stands for the mean concentration of the envelope. Because the interdendritic liquid is assumed to be solutally well mixed, $\bar{C}_e$ is also equal to the liquid/concentration at the solid/liquid interface. Accordingly, the concentration on the solid side, $\bar{C}_{sd}$, is given by

$$\bar{C}_{sd} = \kappa \bar{C}_e(T) \qquad [6]$$

Second, $\varepsilon_k$ is the volume fraction of a phase $k$. Third, $S$ designates the area concentration of an interface, which is defined as the ratio of the interfacial area to the volume of the volume element. Therefore, $S$ represents the inverse of a microscopic length scale. Note that the area concentration of the solid/liquid interface, $S_s$, in dendritic growth is typically much larger than the envelope area concentration, $S_e$. Finally, $\ell_{sd}$ and $\ell_{ld}$ denote the solid and liquid diffusion lengths, respectively. Their physical meanings have been elucidated in Reference 15.

Furthermore, it is worth noting that Eqs. [2] through [5] are nothing else but mass and solute balances. For example, Eq. [3] simply states that the increase in mass of solute in the solid during time $\Delta t$ results from the combined contributions of movement of the solid/liquid interface and solute diffusion across the interface. For negligible back diffusion in the solid, the last term on the right-hand side (RHS) of Eq. [3] drops out. In the growth model for the dendrite tips (*i.e.*, the envelope) of Eq. [2], thermal and curvature undercoolings have been neglected in comparison with solutal undercooling. This is reasonable for most metallic alloys and normal solidification conditions. The assumption also leads to the consequence that the growth kinetic laws for columnar and equiaxed dendrite tips become identical[17,18] and can thus be combined into a single expression. Also, it is realized that the model equations, Eqs. [1] through [5], are equally applicable to columnar and equiaxed dendritic growth, while leaving descriptions of the different characteristics of each mode of solidification to supplementary relations. These include the expressions for the interfacial area concentrations and the diffusion lengths, which have been derived by Wang and Beckermann[15] and are summarized in Table I.

The corresponding boundary and initial conditions to Eqs. [1] through [5] are as follows:

$$-k \frac{\partial T}{\partial x} = h(T - T_a) \text{ (convective cooling)};$$

$$\frac{\partial T}{\partial x} = 0 \text{ (adiabatic condition)} \qquad [7]$$

and

$$\text{at } t = 0, \quad T = T_0, \quad \bar{C}_e = \langle C_l \rangle^l = C_0,$$

$$\langle C_s \rangle^s = \kappa C_0, \quad \varepsilon_s = \varepsilon_{s0}, \quad \varepsilon_d = 0, \quad \varepsilon_l = 1 - \varepsilon_{s0} \qquad [8]$$

where $h$ is the heat transfer coefficient at the chill wall. The initial temperature $T_0$ is not necessarily equal to the liquidus temperature corresponding to the initial concentration, $T_L(C_0)$, and their difference, $\Delta T_0 = T_0 - T_L(C_0)$, represents the pouring superheat. The initial solid fraction $\varepsilon_{s0}$ is a small positive number to account for the finite size of the nuclei present in the liquid melt. In the numerical simulations presented below, $\varepsilon_{s0}$ is chosen to be so small that the later predictions are insensitive to $\varepsilon_{s0}$.

After substituting $\bar{C}_{sd}$ by $\kappa \bar{C}_e$ using Eq. [6], Eqs. [1]

**Table I. Summary of the Supplementary Relations for Equiaxed and Columnar Growth**

| Quantity | Equiaxed Growth | | Columnar Growth |
|---|---|---|---|
| Final radius of dendrite, $R_f$ | $\left(\frac{4}{3}\pi n\right)^{-1/3}$ | | $\lambda_1/\pi^{1/2}$ |
| Solid/Interdendritic liquid interfacial area concentration, $S_s$ | | $\frac{2}{\lambda_2}$ | |
| Envelope area concentration, $S_e$ | $\frac{3(\varepsilon_s + \varepsilon_d)^{2/3}}{R_f \phi_e}$ | | $\frac{2(\varepsilon_s + \varepsilon_d)^{1/2}}{R_f \phi_e}$ |
| Solid diffusion length, $l_{sd}$ | | $\frac{\varepsilon_s \lambda_2}{6(1 - \varepsilon_l)}$ | |
| Liquid diffusion length, $l_{ld}$ | $l_{ld}/R_f = \frac{1}{\mathrm{Pe}}\left\{1 - \frac{3}{\varepsilon_l}\exp \cdot[-\mathrm{Pe}(1-\varepsilon_l)^{1/3}] \cdot \int_{(1-\varepsilon_l)^{1/3}}^{1} x^2 \exp\left[\frac{\mathrm{Pe}(1-\varepsilon_l)^{2/3}}{x}\right] dx\right\}$ (spherical model) | | $l_{ld}/R_f = \frac{1}{\mathrm{Pe}}\left\{1 - \frac{2}{\varepsilon_l}\exp\left[\frac{\mathrm{Pe}}{2} \cdot (1-\varepsilon_l)^{1/2}\ln(1-\varepsilon_l)\right] \cdot \int_{(1-\varepsilon_l)^{1/2}}^{1} x \exp[-\mathrm{Pe}(1-\varepsilon_l)^{1/2}\ln x]\, dx\right\}$ (cylindrical model) |
| | | $\mathrm{Pe} = \bar{w}_{ne} R_f / D_l$ | |

through [5] together with the boundary and initial conditions (Eqs. [7] and [8]) constitute a complete model for five unknowns: $T$, $\varepsilon_s$, $\varepsilon_d$, $\langle C_s\rangle^s$, and $\langle C_l\rangle^l$, while $\bar{C}_e(T)$ is given by the liquidus line of the phase diagram. During the eutectic reaction, both the temperature and the interfacial liquid concentration are fixed at certain values given by the phase diagram so that the solid volume fraction can be determined from the energy equation. The liquids in the interdendritic and extradendritic regions are then transformed into the eutectic phase (neglecting any eutectic undercooling).

### B. *Grain Nucleation, Growth, and Morphology*

The supplementary relations to Eqs. [2] through [5], as summarized in Table I, require the knowledge of the nuclei density of equiaxed grains, the coefficients in the growth kinetic law, and the primary and secondary dendrite arm spacings. For simplicity, a certain average nuclei density is assumed to prevail throughout the equiaxed zone, with nucleation taking place instantaneously at the liquidus temperature. The value of the nuclei density is varied to explore its effect on the CET. In the experiments used for validation of the present model (see below), detailed measurements of the nuclei density or grain size distribution in the equiaxed zone have not been provided, making a selection of a more realistic nucleation law difficult. It should be mentioned that a variable nuclei density, as given by the instantaneous nucleation law attributed to Stefanescu *et al.*,[19] has been used in Reference 15, and other nucleation laws can be implemented without difficulty.

Approximating the dendrite tip by a paraboloid of revolution, a growth model for dendrite tips has been derived by Kurz *et al.*[17] and Lipton *et al.*[18] that involves a complicated Ivantsov function. For computational convenience, the inverse Ivantsov function needed in the present model (*i.e.*, Eq. [2]) has been closely approximated by the following correlation:

$$\mathrm{Iv}^{-1}(\Omega) = a\left(\frac{\Omega}{1-\Omega}\right)^b \qquad [9]$$

where $a = 0.4567$ and $b = 1.195$ give the best fit.[16]

The primary dendrite arm spacing in columnar growth can be predicted from the theory developed by Hunt:[20]

$$\lambda_1 = [64\Gamma D_l m_l (1-\kappa) C_0]^{1/4} G^{-1/2} V_t^{-1/4} \qquad [10]$$

Kurz and Fisher's theory[21] results in the same equation, except for a different numerical constant. The secondary dendrite arm spacing is primarily dictated by the cooling rate *via* coarsening phenomena. Here, the following commonly used relationship is employed:

$$\lambda_2 = a\dot{T}^{-1/3} \qquad [11]$$

where $\lambda_2$ is the secondary arm spacing (in micrometers), $a$ is a proportionality constant, and $\dot{T}$ is the cooling rate (in Kelvin per second). Jones[22] suggests that $a = 50$ for Al-Cu and Al-Si alloys through correlating data from a wide range of sources. The thermal gradient $G$, cooling rate $\dot{T}$, and growth velocity $V_t$ are instantaneously and locally evaluated from the calculated temperature field.

## III. NUMERICAL PROCEDURES

Equations [1] through [5] are intricately coupled, and their numerical solution needs special attention. The spatial derivative is only seen in the energy equation. On

the other hand, a time dependence is present in all equations, but the various dependent variables have different evolution rates. As noted by Rappaz and Thevoz,[23] the temperature and solid fraction evolve much more slowly than the grain nucleation and growth, which are governed by the nucleation and growth kinetic laws. Therefore, a large time step is desirable for Eq. [1], particularly in 2-D and three-dimensional (3-D) situations, whereas a very fine time step is needed for numerically capturing the nucleation growth stage. A two time-step coupling scheme, inspired by Thevoz *et al.*,[24] is thus proposed to resolve the problem.

### A. *Two Time-Step Scheme*

In the two time-step coupling scheme, a fully implicit control volume-based finite-difference method is employed to solve the energy equation, Eq. [1]. The details of the method can be found in Reference 25. The last term on the RHS of Eq. [1] is treated as a source term, which is first guessed (from the previous time-step) and then calculated by solving Eqs. [2] through [5]. The implicit nature of the algorithm allows for a relatively large time step, $\Delta t$, while maintaining a high accuracy of the results. Next, a much smaller time-step, $\delta t = \Delta t/N$, is employed to integrate Eqs. [2] through [5] by simple time marching, where it is assumed that the enthalpy, consisting of both sensible and latent heats, changes linearly during the time interval $\Delta t$. Hence, the enthalpy variation during each smaller time-step, $\delta t$, is equal to the enthalpy change during the large time-step divided by $N$. The total variation in the solid fraction during the large time-step, $\Delta t$, as calculated from the solute diffusion model, is fed back to the energy equation for correction of the temperature field. This process is repeated until convergence is achieved. Experience shows that $N = 10$ already gives satisfactory results. The flowchart shown in Figure 2 illustrates the scheme and the interactions between the two time-step levels. The present scheme modifies the one proposed by Thevoz *et al.*,[24] because it allows for a complete coupling between the heat and solute diffusion processes; however, the scheme by Thevoz *et al.* does not feed the calculated solid fraction variation back into the energy equation for rectifying the temperature field. Therefore, the present scheme eliminates the stability and convergence problems encountered in Reference 24. The present scheme also improves the one recently proposed by Tseng *et al.*,[26] in which the temperatures on the two time-step levels are not related to each other.

### B. *Columnar Front Tracking*

Tracking of the columnar front serves to distinguish the columnar and equiaxed subregions so that the corresponding supplementary relations can be specified. In addition, it enables the capture of the columnar-to-equiaxed transition, which is of primary interest in the present study.

The tracking of the columnar front is based on the fact that at the columnar front, the isotherm velocity is equal to the dendrite-tip growth velocity at the same location. Because of solutal undercooling in the extradendritic liquid, the temperature at the columnar front, $T_{cf}$, is no longer

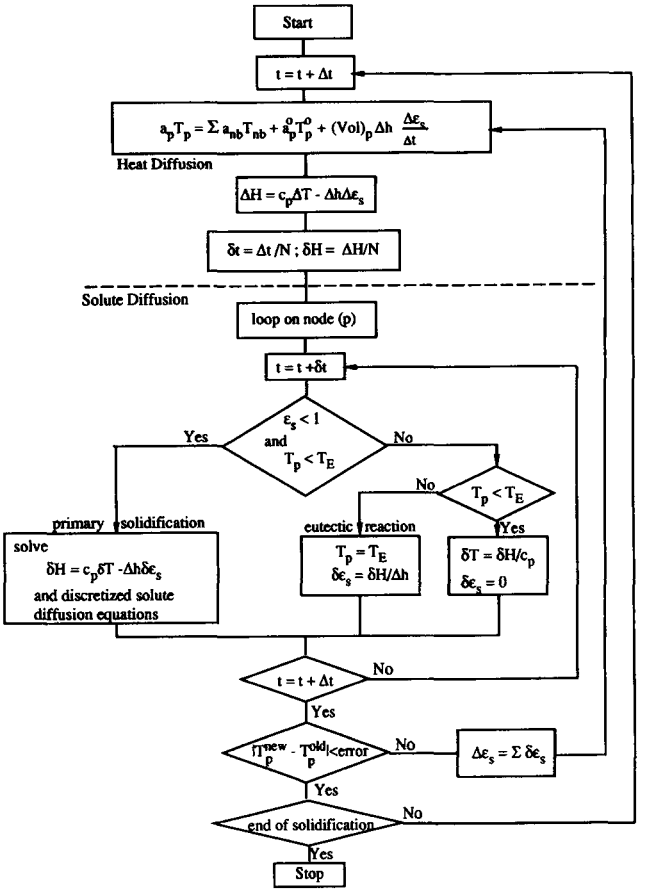


Fig. 2—Flowchart of the two time-step scheme for coupled heat and solute diffusion.

equal to the liquidus temperature corresponding to $C_0$, but instead, it needs to be determined in an iterative procedure. This procedure is first explained for the 1-D case and then extended to multidimensional situations.

Consider the 1-D case shown in Figure 1. First, the front velocity is calculated using the growth kinetic law (Eq. [9]) by assuming a trial front temperature, $T^n_{cf}|_0$, at the present time-step, *i.e.*,

$$V^n_{cf} = f[T_L(C_0) - T^n_{cf}|_0] \qquad [12]$$

The columnar front at this time is then located at

$$x^n_{cf} = x^{n-1}_{cf} + V^n_{cf}\,\Delta t \qquad [13]$$

After determining the front location, a new front temperature, $T^n_{cf}|_1$, can be obtained from the computed temperature field. The process is repeated until convergence is achieved. This tracking algorithm is implicit in nature, making it possible to use a relatively large time-step in combination with the implicit finite-difference scheme for the heat-conduction equation.

The previous front-tracking technique can be straightforwardly applied to multidimensional situations. But, the procedure may become extremely tedious and require large computational times, because a number of points need to be tracked to form a continuous columnar front in a multidimensional domain. To avoid this difficulty, it is assumed in the present study that the columnar front lies on a single isotherm of a yet unknown

**Table II. Physical Properties of Al-Cu and Sn-Pb Alloys[12,28–30]**

| Quantity | Symbol | Al-Cu | Sn-Pb | Unit |
|---|---|---|---|---|
| Eutectic concentration | $C_E$ | 33.2 | 38.1 | (wt pct) |
| Eutectic temperature | $T_E$ | 821 | 456 | (K) |
| Melting point of pure metal | $T_m$ | 933 | 505.1 | (K) |
| Partition coefficient | $\kappa$ | 0.17 | 0.096 | (−) |
| Liquidus slope | $m_l$ | −3.37 | −1.29 | (K/wt pct) |
| Gibbs-Thomson coefficient | $\Gamma$ | $2.41 \times 10^{-7}$ | $0.775 \times 10^{-7}$ | (mK) |
| Volumetric latent heat | $\Delta h$ | $1.02 \times 10^{9}$ | $4.35 \times 10^{8}$ | ($J/m^3$) |
| Volumetric specific heat | $c_p$ | $3.4 \times 10^{6}$ | $1.925 \times 10^{6}$ | ($J/m^3 \cdot K$) |
| Diffusion coefficient | $D_l$ | $5.0 \times 10^{-9}$ | $3.0 \times 10^{-9}$ | ($m^2/s$) |
| | $D_s$ | 0.0 (assumed) | | ($m^2/s$) |
| Thermal conductivity | $k_l$ | 77 | 20 | (W/mK) |
| | $k_s$ | 153 | 40 | (W/mK) |

temperature. The assumption is physically sound because the columnar grains grow in the preferred direction that is closest to the heat-flow direction and are constrained by the movement of isotherms. With this assumption in mind, the front tracking in a multidimensional field can be accomplished by tracing one particular point on a columnar front. Hence, the same procedure as for the 1-D case applies, in addition to taking account of the growth angle, $\alpha$, which is assumed to coincide with the heat-flow direction. For instance, in a 2-D domain, the front point $(x, y)$ at the time-step $n$ can be iteratively computed by

$$x_{cf}^n = x_{cf}^{n-1} + (V_{cf}^n \cos \alpha)\, \Delta t \qquad [14]$$

$$y_{cf}^n = y_{cf}^{n-1} + (V_{cf}^n \sin \alpha)\, \Delta t \qquad [15]$$

where the angle, $\alpha$, is given by

$$\alpha = \tan^{-1}\left(\frac{\partial T/\partial x}{\partial T/\partial y}\right) \qquad [16]$$

Once the single point and the tip temperature are iteratively determined, the whole columnar front can be constructed by identifying the corresponding isotherm. This procedure to deal with multidimensional front tracking is easy and efficient to implement and has been thoroughly tested and found to be stable in 2-D cases. In more complex solidification situations where melt convection and solid movement are present, a more advanced scheme needs to be devised to track a nonisothermal CET interface.

### C. *Eutectic Reaction*

When the temperature approaches the eutectic value in a control volume, the large source-term technique proposed by Voller[27] is used to fix the nodal temperature at the eutectic value and to simultaneously update the solid fraction from the energy equation.

## IV. RESULTS AND DISCUSSION

The multiphase model described in Section II is applied to Al-3 wt pct Cu and Sn-5, and 10, 15 wt pct Pb alloys, whose physical properties are listed in Table II. The solid diffusion coefficient, $D_s$, is set to zero, implying that back diffusion in the solid is neglected. Calculations are performed for both 1-D and 2-D ingots using the numerical procedures outlined in Section III. The ambient (coolant) temperature, $T_a$, is chosen as 293 K for all calculations presented in Section A. The grid size of the computational mesh for all results reported in this section is 2.5 mm (*i.e.*, 42 grids in a 100-mm-long ingot). The larger time-step is initially 1 and 0.25 seconds for the Al-Cu and Sn-Pb alloys, respectively, and doubled during the later stages of solidification. The smaller time-step used for integration of the solute diffusion equations is exactly one order of magnitude smaller than the larger time-step. These grid and time step sizes were determined through a test of grid size and time-step independence, which is summarized in Table III. It can be seen that the convergence of the CET position with respect to both grid size and time-step is excellent. Although the code was not optimized, the computational time is modest.

### A. *Numerical Results*

A representative 1-D simulation is first carried out for an Al-3 wt pct Cu alloy in a 1-D mold of 100-mm length, and the results are presented in Figures 3 and 4. The conditions are $h = 65$ W/m$^2$ K, $n = 10^5$ m$^{-3}$, and $\Delta T_0 = 20$ K.

**Table III. Test of Time-Step and Grid Size Independence for a 100-mm-Long Al-3 Weight Percent Cu Casting: $h = 65$ W/m$^2$ K, $\Delta T_0 = 20$ K, and $n = 10^5$ m$^{-3}$**

| Grid Size (mm) | Time-Step (s) | CET Position (Dimensionless) | CPU Time* (s) |
|---|---|---|---|
| | 4 | 0.4560 | 150 |
| 2.5 | 2 | 0.4528 | 180 |
| | 1 | 0.4513 | 250 |
| | 0.5 | 0.4519 | 540 |
| 10 | | 0.5272 | 100 |
| 5 | | 0.4644 | 150 |
| 2.5 | 1 | 0.4513 | 250 |
| 1.67 | | 0.4434 | 360 |
| 1.25 | | 0.4412 | 480 |

*On an Apollo-DN 10,000 workstation, until the CET position is established ($t \approx 650$ s).

Figure 3(a) shows the calculated cooling curves at five locations between $x/L = 0.025$ and 0.825 with an interval of 0.2. Negligible bouncing or reheating effects are seen in the cooling curves near the recalescence stage (see the inset of Figure 3(a)), although a relatively coarse grid is used in the present study. Significant recalescence is only observed in the first curve for the location nearest to the chill wall, whereas the other curves exhibit thermal plateaus. It can be concluded that for the mixed mode of solidification, recalescence is less pronounced than in purely equiaxed solidification.[24] This is because the cooling curve for mixed growth embodies features of columnar solidification, namely, a temperature plateau in the cooling curve.[7] The fact that the cooling curves for various modes of solidification are distinctive in shape has been used by Lipton *et al.*[31] for *in situ* measurements of the CET positions in castings.

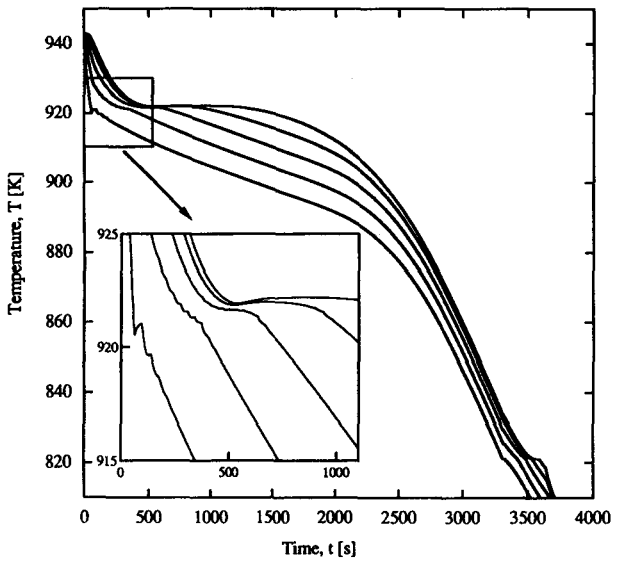


(*a*)

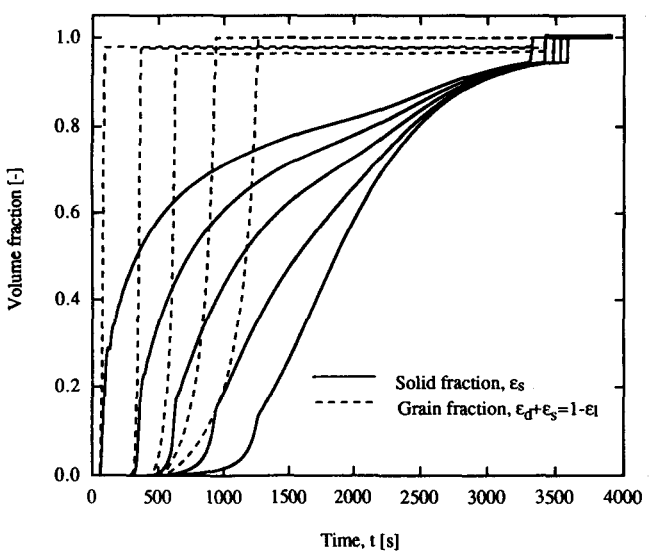


(*b*)

Fig. 3—(*a*) Cooling curves and (*b*) solid and grain volume fraction evolutions for a 1-D casting of an Al-3 wt pct Cu alloy ($h = 65$ W/m$^2$ K, $n = 10^5$ m$^{-3}$, and $\Delta T_0 = 20$ K). The curves from left to right correspond to five locations between $x/L = 0.025$ and 0.825 with an interval of 0.2.

The computed solid and grain fractions are displayed in Figure 3(b) at the same locations as the cooling curves. The grain fraction is defined as the sum of the solid and interdendritic liquid volume fractions. It is now clear that the two quantities do evolve at disparate rates, as mentioned in Section III. Hence, a two time-step scheme is necessary for accurate calculations of both macro- and microscopic features of solidification. In addition, it is noticed from Figure 3(b) that the grain fraction at some locations does not reach the maximum value of unity. This is because complete mixing of solute in the extradendritic region is reached before the grain envelopes impinge. In other words, the dendrite tips do not advance further, because undercooling at the tips is no longer significant. The remaining liquid in the extradendritic region is ultimately solidified during the eutectic reaction.

The evolution of the different regions in the ingot is depicted in Figure 4, where the dashed line denotes the liquidus isotherm corresponding to the initial alloy concentration, and the solid line stands for the CET interface that divides the mushy zone into the columnar and equiaxed regions. The final CET position corresponds to the vertical part of the solid line. Hence, the CET occurs about 650 seconds after the initiation of cooling of the ingot.

Selected 2-D simulations are also performed for the Al-3 wt pct Cu alloy. Figures 5(a) and (b) depict the evolution of the interface between the columnar and equiaxed zones in 100 × 100-mm square and 50 × 100-mm rectangular castings, respectively. The left and bottom walls are cooled with a heat-transfer coefficient of 65 W/m$^2$ K, while the upper and right boundaries are insulated to represent symmetry conditions. Other conditions are the same as in the 1-D simulation. The predicted CET interfaces are quite similar to the ones observed in the experiments of Brown and Spittle[32] for the square geometry and to the simulation results obtained by Zhu and Smith[10] for the rectangular geometry.

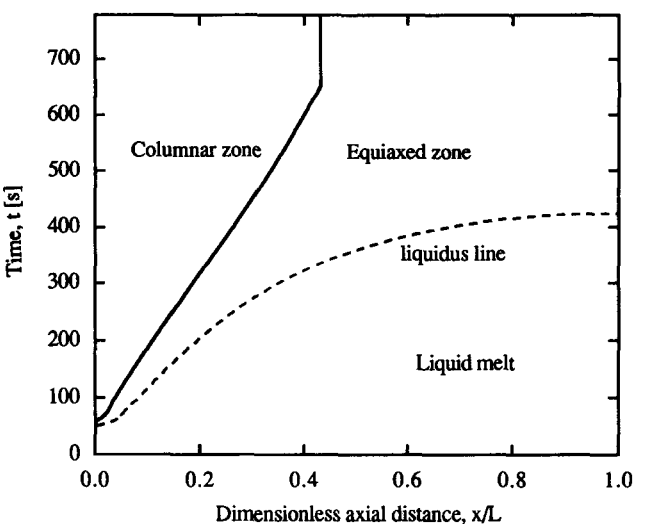


Fig. 4—Map of different regions developing in a 1-D casting of an Al-3 wt pct Cu alloy ($h = 65$ W/m$^2$ K, $n = 10^5$ m$^{-3}$, and $\Delta T_0 = 20$ K).

B. *Experimental Verification*

This section focuses on validating the present multiphase model using the experimental data of Weinberg and co-workers for both Sn-Pb[12] and Al-Cu[13] alloys. In Weinberg's experiments, the various alloys are poured into a 100-mm-long cylindrical mold and solidified vertically upward from a water-cooled copper chill at the bottom. One-dimensional solidification results by avoiding lateral heat losses. The CET position is observed and measured by sectioning the solidified ingots along the vertical center plane and polishing and etching the sectioned surface. Since for both alloys the solute-rich interdendritic liquid has a higher density than the overlying alloy melt and the axial temperature gradients are stable, melt convection owing to buoyancy forces is minimal, and thus, the CET data are well suited for comparison with the present model where convection is omitted. Some uncertainties remain, however, with respect to the effects of sedimentation or floating of equiaxed grains as a result of the density difference between the solid and liquid phases.

A comparison between model predictions and experimental measurements of the CET is first attempted for Sn-Pb alloys. Corresponding experimental data are taken from the study of Mahapatra and Weinberg,[12] which covers a wide range of chill heat-transfer coefficients, pouring superheats, and alloy compositions. Most of the important parameters were explicitly reported in Reference 12, except for such metallurgical parameters as the secondary and primary dendrite arm spacings and the equiaxed nuclei density. The secondary dendrite arm spacing, $\lambda_2$, is not needed in the present calculations because back diffusion in the solid is neglected and the interdendritic liquid is assumed to be solutally well mixed. The primary arm spacing, $\lambda_1$, is adequately calculated by Eq. [10], although a direct confirmation of this equation through the experimental data in Reference 12 is not possible. In fact, a few numerical tests (not shown here), in which $\lambda_1$ was artificially changed, indicate that the CET prediction is relatively insensitive to the primary dendrite arm spacing in the columnar region. Extreme care, however, needs to be taken in selecting values for the equiaxed nuclei density. In the absence of a reliable nucleation model, it is instructive to first numerically explore the effect of the equiaxed nuclei density on the CET for the experimental conditions of Reference 12. Based on these model studies, a single nuclei density is then selected for quantitative comparison with the experimental data.

Figures 6 through 8 show the effect of the equiaxed nuclei density on the CET position as a function of the chill heat-transfer coefficient, pouring superheat and alloy composition, respectively. A base case has been defined as $C_0$ = 10 wt pct, $h$ = 120 W/m$^2$ K, and $\Delta T_0$ = 10 K. Figures 6 through 8 indicate that the nuclei density has a remarkable effect on the CET position. For all solidification conditions, the CET occurs, as expected, at a shorter distance from the chill as the nuclei density in the equiaxed zone is increased.

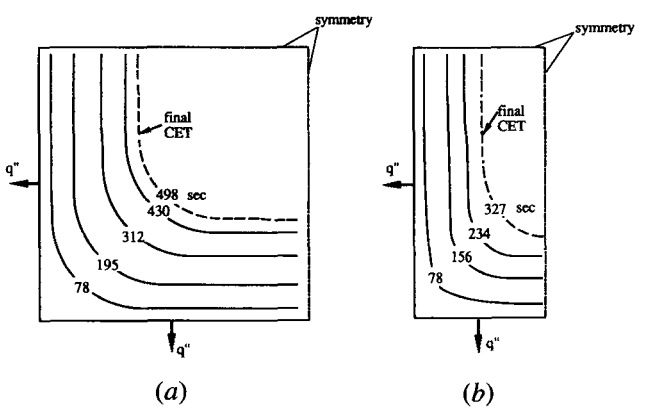


Fig. 5—Evolution of the interface between the columnar and equiaxed zones in (*a*) 100 × 100-mm square and (*b*) 50 × 100-mm rectangular castings of an Al-3 wt pct Cu alloy ($h$ = 65 W/m$^2$ K, $n$ = $10^5$ m$^{-3}$, and $\Delta T_0$ = 20 K). The dashed line denotes the final CET position.

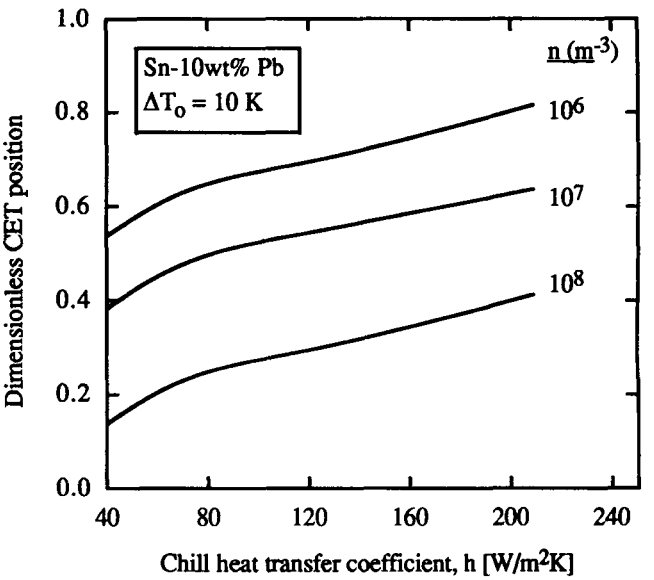


Fig. 6—Effects of nuclei density and chill heat-transfer coefficient on the CET position in a 1-D casting of an Sn-10 wt pct Pb alloy.

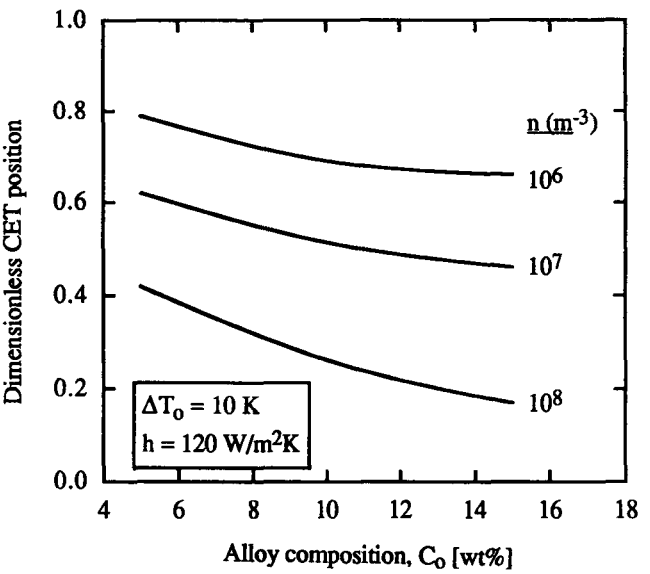


Fig. 7—Effects of nuclei density and alloy composition on the CET position in a 1-D casting of Sn-Pb alloys.

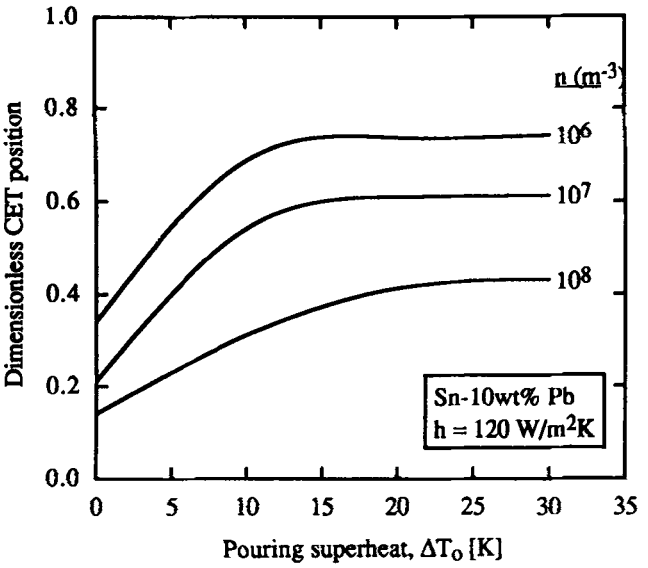


Fig. 8—Effects of nuclei density and pouring superheat on the CET position in a 1-D casting of an Sn-10 wt pct Pb alloy.

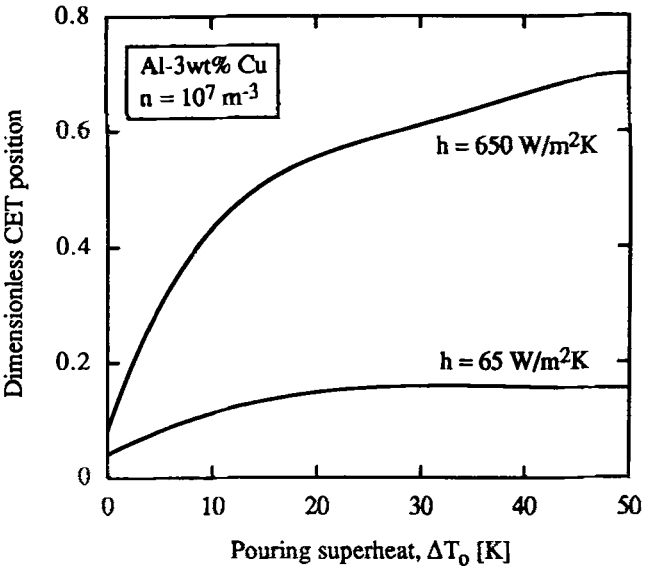


Fig. 9—Effects of chill heat-transfer coefficient and pouring superheat on the CET position in a 1-D casting of an Al-3 wt pct Cu alloy.

Figure 6 further displays the effect of the chill heat-transfer coefficient, $h$, on the CET position for various equiaxed nuclei densities. It can be seen that a large heat extraction rate at the chill favors the development of the columnar region, at the expense of the equiaxed zone, which is in qualitative agreement with the experimental observations.[12] This is because the steep thermal gradient resulting from the large heat extraction rate narrows the equiaxed region ahead of the columnar front and thus impedes equiaxed growth. Also, the variation of the CET position with $h$ is approximately the same for all nuclei densities.

The effect of alloy composition on the CET is shown in Figure 7 for different equiaxed nuclei densities. The length of the columnar zone increases with decreasing solute concentration. In the limiting case of a pure metal, columnar growth can be expected to prevail throughout the casting. Interestingly, the sensitivity of the CET position on the alloy composition increases with increasing equiaxed nuclei density.

The dependence of the CET position on the pouring superheat, $\Delta T_0$, is investigated in Figures 8 and 9. The superheat effect for the Sn-Pb alloy is seen to be pronounced only at low superheats and diminishes in an asymptotic manner at higher pouring temperatures. A physical explanation can be obtained by examining the temperature distribution during solidification. Due to the relatively low thermal conductivity of the Sn-Pb alloys, the initial superheat is not completely dissipated before solidification starts. As a result, the equiaxed zone ahead of the columnar front is narrowed by the remaining superheat, and the columnar growth is blocked at a later time. The predicted insensitivity of the CET to the superheat for $\Delta T_0 \geq 10$ K is in qualitative agreement with the experiments,[12] and the predicted decrease in the CET position for lower superheats has been observed in other experiments.[1] Also note that the sensitivity of the CET position on the pouring superheat decreases for large equiaxed nuclei densities (*e.g.*, $n = 10^8$ m$^{-3}$).

The superheat effect was, however, found to be quite significant in the experiments of Suri *et al.*[33] for an Al-4.5 wt pct Cu alloy. In these experiments, the cooling rates were about one order of magnitude higher than those in Ziv and Weinberg's experiments.[13] To explain the apparent discrepancy in the experimental observations, Figure 9 compares numerical predictions of the CET position for two disparate chill heat-transfer coefficients. The low $h$ corresponds to Ziv and Weinberg's experiments, while the high $h$ is intended to be representative of the conditions in Suri's experiments. It can be seen that while the superheat effect is insignificant for the low-chill heat-transfer coefficient, it is indeed substantial for the large cooling rate. A physical explanation can be found from the temperature distribution produced by the fast cooling: the initial large superheat is not fully dissipated before rapid columnar growth occurs, and the remaining superheat thus hinders equiaxed growth and leads to a significant delay of the CET. Here, it should be mentioned again that the present analysis does not consider convection. In general, dendrite fragmentation and grain multiplication owing to convection can influence the CET, and the extent of convection can be expected to depend on superheat.

The previous parametric studies indicate that the equiaxed nuclei density is one of the most important factors in determining the CET. Despite the absence of a reliable nucleation model and suitable grain size measurements, a quantitative comparison with the experimental CET data reported in Reference 12 is attempted in the following. For this purpose, it is assumed that a single mean equiaxed nuclei density can be found that is representative of the 24 experimental runs in Reference 12. Based on the parametric studies, it is found that a nuclei density, $n$, of $10^7$ m$^{-3}$ results in a match of the predicted and measured CET positions to within 20 pct. A summary of this comparison for all cases investigated by Mahapatra and Weinberg is presented in Table IV and also illustrated in Figure 10. Again, the value of $10^7$ m$^{-3}$ is chosen to produce good overall

**Table IV. Comparison of Measured[12,13] and Predicted CET Positions for Al-Cu ($n = 10^5$ m$^{-3}$) and Sn-Pb ($n = 10^7$ m$^{-3}$) Alloys**

| Case Number | Superheat (K) | Heat-Transfer Coefficient (W/m$^2$ K) | Measured CET Position (mm) | Predicted CET Position (mm) | Relative Error (Pct) |
|---|---|---|---|---|---|
| *Sn-10 Wt Pct Pb* | | | | | |
| 1 | 11.5 | 63 | 38 | 45.9 | 17.2 |
| 2 | 11.5 | 113 | 60 | 53.7 | −11.7 |
| 3 | 11.5 | 134 | 65 | 56.3 | −15.5 |
| 4 | 19 | 63 | 40 | 48.7 | 17.8 |
| 5 | 19 | 84 | 45 | 55.8 | 19.4 |
| 6 | 19 | 134 | 65 | 63.3 | −2.7 |
| 7 | 31 | 63 | 35 | 51.2 | 31.6 |
| 8 | 31 | 96 | 50 | 58.7 | 14.8 |
| 9 | 31 | 113 | 57 | 62.3 | 8.5 |
| 10 | 31 | 134 | 65 | 65.8 | 1.2 |
| 11 | 31 | 251 | none | 76.1 | <−23.9 |
| 12 | 36 | 96 | 50 | 60.9 | 17.9 |
| 13 | 36 | 134 | 65 | 66 | 1.52 |
| 14 | 36 | 209 | 80 | 71.3 | −12.2 |
| 15 | 41 | 301 | none | 78.7 | <−21.3 |
| *Sn-5 Wt Pct Pb* | | | | | |
| 16 | 7.5 | 71 | 52 | 46.3 | −12.3 |
| 17 | 12 | 92 | 60 | 58.4 | −2.7 |
| 18 | 12 | 146 | none | 72.1 | <−27.9 |
| 19 | 22 | 113 | 70 | 66 | −6.1 |
| *Sn-15 Wt Pct Pb* | | | | | |
| 20 | 21.5 | 151 | 48 | 58.6 | 18.1 |
| 21 | 21.5 | 167 | 55 | 63.5 | 13.4 |
| 22 | 21.5 | 272 | 70 | 71.2 | 1.7 |
| 23 | 36 | 105 | 40 | 50.1 | 20.2 |
| 24 | 41 | 146 | 50 | 60.8 | 17.7 |
| *Al-3 Wt Pct Cu* | | | | | |
| 25 | 20 | 95 | 72 | 58.6 | −18.6 |
| 26 | 20 | 65 | 53 | 46.4 | −14.2 |
| 27 | 20 | 65 | 53 | 46.4 | −14.2 |
| 28 | 20 | 63 | 48 | 46.1 | −4.1 |
| 29 | 20 | 63 | 48 | 46.1 | −4.1 |
| 30 | 20 | 50 | 37 | 39 | 5.1 |
| 31 | 20 | 53 | 45 | 41 | −9.8 |
| 32 | 20 | 53 | 45 | 41 | −9.8 |
| 33 | 20 | 37 | 34 | 36 | 5.6 |

*Pouring superheats were not available in the experiments for the Al-3 wt pct Cu alloy, and the value of 20 K is assumed for calculations.

agreement with the measured CET data, and it is an adjustable constant. Nonetheless, the good agreement for a variety of alloy compositions and solidification conditions suggests that the present model is indeed capable of predicting the CET quantitatively, given an accurate nucleation model. Furthermore, it is noticed that the value of $n = 10^7$ m$^{-3}$ (which corresponds to a final equiaxed grain size of about 2.8 mm) is of a reasonable magnitude, although some variations can be expected for the different cases.

The remaining discussion focuses on comparing the model predictions to a set of experimental data for an Al-3 wt pct Cu alloy obtained more recently by Ziv and Weinberg,[13] where the effect of the chill heat-transfer coefficient on the CET was explored. Figure 11 shows that for all chill heat-transfer coefficients the present predictions agree fairly well with the experimental data for a nuclei density in the equiaxed zone of $10^5$ m$^{-3}$. However, actual average nuclei densities observed in these experiments are reported to remain virtually constant at about $5 \times 10^6$ m$^{-3}$ (corresponding to a grain size between 5.4 and 7.2 mm), regardless of the cooling conditions.[13] In order to examine possible causes for this discrepancy, the instantaneous nucleation law owing to Stefanescu *et al.*[19] was tried for selected cases. This law reflects the dependence of the nuclei density on the solidification rate and, thus, predicts a variable nuclei density in a casting. Calculations (not reported here), however, indicate that the predicted CET position, for the same average equiaxed nuclei density, is only slightly affected by the choice of the nucleation law. Attempts at resolving the discrepancy by using other, more sophisticated, nucleation models proved to be unsuccessful, because of our inability to determine the many empirical constants contained in these models from the experimental data provided.[13] Certainly, this topic requires additional research attention. Some of the discrepancy can be attributed to variations of the heat-transfer coefficient at the mold/metal interface during the experiments and lateral heat losses, as noted by Ziv and

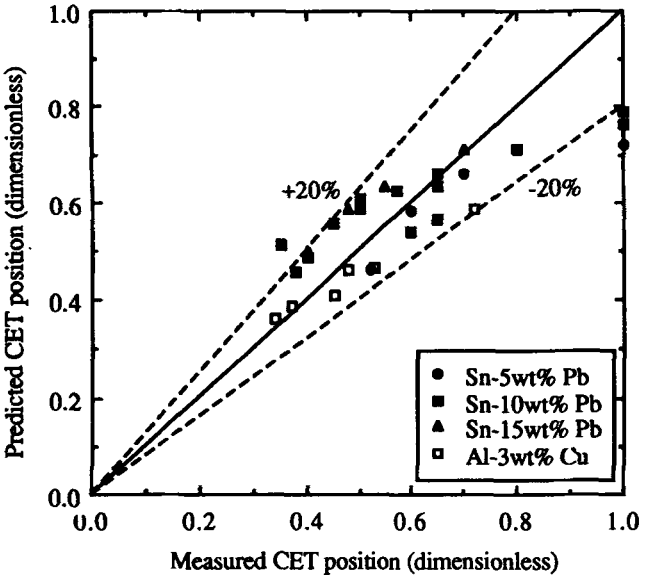


Fig. 10—Comparison of the predicted CET positions with all experimental data reported in References 12 and 13 (Sn-Pb alloys: $n$ = $10^7$ $m^{-3}$; Al-3 wt pct Cu alloy: $n$ = $10^5$ $m^{-3}$).

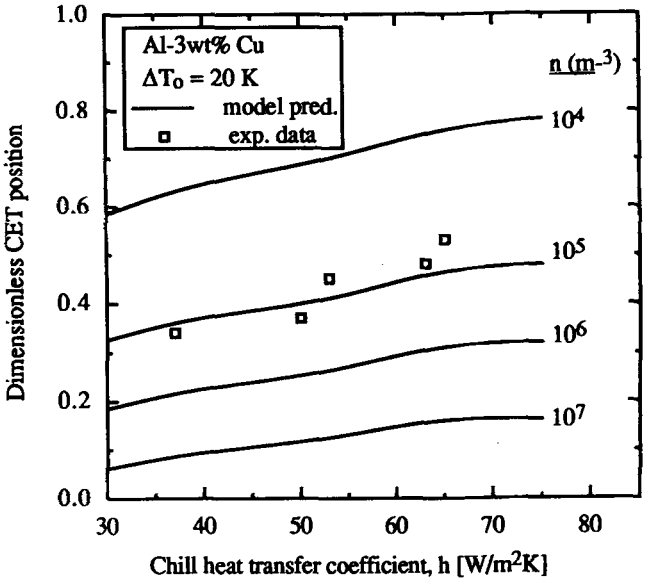


Fig. 11—Effects of nuclei density and chill heat-transfer coefficient on the CET position in a 1-D casting of an Al-3 wt pct Cu alloy. Comparison with Ziv and Weinberg's data.[13]

Weinberg. In fact, attempts by Ziv and Weinberg to simulate the cooling curves using a 1-D heat-transfer model were noted to be unsuccessful because of an incomplete knowledge of the thermal boundary conditions in the experiments. The above comparison for the Al-3 wt pct Cu alloy using an equiaxed nuclei density of $10^5$ $m^{-3}$ in the calculations is also included in Table IV and Figure 10.

Figure 11 can also be used to examine the effect of inoculation on the CET. In the inoculation experiments[13] with $h$ = 50 W/m$^2$ K, it was found that the equiaxed grain size decreases from 5.4 to 1 mm by adding 172 ppm of $TiB_2$ to the liquid melt. The 1-mm grain size corresponds to an equiaxed nuclei density of about $1.9 \times 10^9$ $m^{-3}$. Figure 11 shows that, at this value of the nuclei density and $h$ = 50 W/m$^2$ K, a wholly equiaxed structure is predicted, which agrees with the experimental observations.[13] In fact, Figure 11 indicates that the transition to a wholly equiaxed structure takes place at a nuclei density of roughly $10^8$ $m^{-3}$.

Figure 12 compares the theoretical predictions with experimental data of the actual time when the CET occurs from the start of solidification. This CET time was measured in Ziv and Weinberg's experiments[13] to obtain the apparent columnar dendrite tip velocity $V_t$. Now, the values of $V_t$ reported in Table I of Reference 13 are converted back to CET times and are displayed in Figure 12 together with the theoretical predictions. As can be seen, good agreement is achieved, although the data show little variations because of the narrow range of the heat-transfer coefficient covered in these experiments. The only point that substantially deviates from the model was identified as a questionable datum by the authors.[13] The fact that both the CET position and time are fairly well predicted indicates that the growth model for dendrite tips used in the present study is appropriate. In addition, it is noticed that the CET time slightly decreases as the heat-transfer coefficient increases.

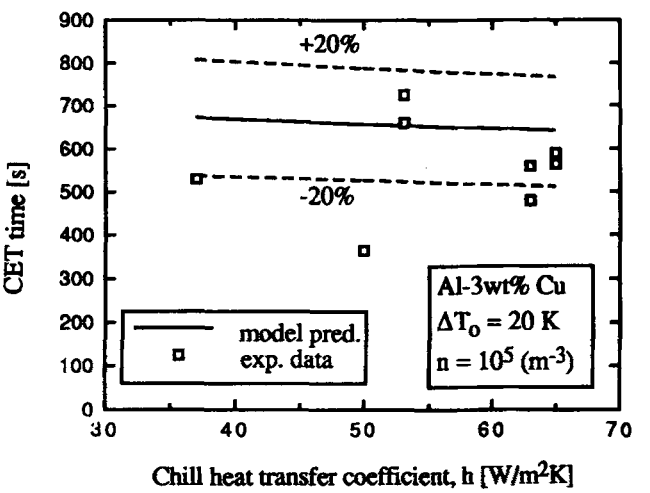


Fig. 12—Comparison of measured[13] and predicted CET times in a 1-D casting of an Al-3 wt pct Cu alloy.

## V. CONCLUSIONS

The following major conclusions are derived from the present study.

1. A comprehensive model that accounts for grain nucleation, growth, and morphology, as well as solute and heat diffusion is proposed for the prediction of the CET in multi-dimensional castings.
2. An implicit, single-domain numerical algorithm is developed to calculate both micro- and macroscopic features of solidification. A novel front tracking technique is proposed to capture the CET dynamically.
3. The effects of alloy composition, pouring superheat, density of nucleation sites in the bulk liquid, and cooling rate at the mold wall are investigated for a 1-D casting. Representative results are given for 2-D castings. Knowledge of the equiaxed nuclei density

is particularly crucial in a quantitative prediction of the CET.

4. For several Sn-Pb[12] and Al-Cu[13] alloys and a wide variety of solidification conditions, it is demonstrated that, given a realistic nucleation model, quantitative agreement between measured and calculated CET positions can be obtained using the present model.
5. More well-controlled experiments are needed to fully validate the present model. The measurement of the equiaxed grain size and distribution together with an accurate knowledge of the thermal boundary conditions should receive particular attention.
6. Melt convection and crystal multiplication/transport remain to be included for situations where diffusion is not dominating.

## NOMENCLATURE

| | |
|---|---|
| $a$ | constant in Eq. [11], m $(K/s)^{1/3}$ |
| $C$ | concentration of a chemical species, wt pct |
| $c_p$ | volumetric specific heat, $J/m^3 \cdot K$ |
| $D$ | mass diffusion coefficient, $m^2/s$ |
| $G$ | temperature gradient, K/m |
| $h$ | chill heat-transfer coefficient, $W/m^2 \cdot K$ |
| $H$ | enthalpy, $J/m^3$ |
| Iv | Ivantsov function |
| $k$ | thermal conductivity, $W/m \cdot K$ |
| $\ell$ | solute diffusion length, m |
| $L$ | casting length, m |
| $m_l$ | liquidus line slope, K/wt pct |
| $n$ | equiaxed nuclei density, $m^{-3}$ |
| Pe | envelope Peclet number, $\bar{w}_{ne}R_f/D_l$ |
| $Pe_t$ | tip Peclet number, $V_tR_t/(2D_l)$ |
| $R$ | radius, m |
| $S$ | interfacial area concentration, $m^{-1}$ |
| $t$ | time, s |
| $T$ | temperature, K |
| $\dot{T}$ | cooling rate, $dT/dt$, K/s |
| $V_t$ | dendrite tip velocity, m/s |
| $\bar{w}_{ne}$ | envelope velocity, m/s |
| $x$ | axial distance, m |
| $y$ | coordinate, m |

### Greek Symbols

| | |
|---|---|
| $\alpha$ | angle of columnar grains with respect to the axial direction |
| $\Gamma$ | Gibbs-Thomson coefficient in the growth model for dendrite tips, $kg/m^3 \cdot s$ |
| $\delta t$ | smaller time step, s |
| $\Delta h$ | latent heat of phase change, $J/m^3$ |
| $\Delta t$ | larger time step, s |
| $\Delta T_0$ | pouring superheat, $T_0 - T_L(C_0)$, K |
| $\Delta T_N$ | nucleation undercooling, K |
| $\varepsilon$ | volume fraction |
| $\kappa$ | partition coefficient, wt pct/wt pct |
| $\lambda$ | dendrite arm spacing, $\mu$m |
| $\phi_e$ | shape factor of the dendrite envelope, $\phi_e = 1$ in this article |
| $\Omega$ | solutal supersaturation, $(\bar{C}_e - \langle C_l \rangle^l)/[\bar{C}_e(1 - \kappa)]$ |

### Subscripts

| | |
|---|---|
| $a$ | ambient |
| $cf$ | columnar front |
| $d$ | interdendritic liquid |
| $e$ | dendrite envelope |
| $E$ | eutectic point |
| $f$ | final |
| $l$ | extradendritic liquid |
| $L$ | liquidus |
| $ld$ | extradendritic/interdendritic liquid interface |
| $m$ | melting point of pure metals |
| $nb$ | neighboring coefficients in the discretized energy equation, see Patankar[25] |
| 0 | initial state |
| $p$ | nodal point |
| $s$ | solid |
| $sd$ | solid-interdendritic liquid interface |
| $t$ | dendrite tip |

## ACKNOWLEDGMENTS

This work was supported by the National Science Foundation under Grant No. CTS-8957149, the National Aeronautics and Space Administration under Grant No. NCC3-290, and the ALCOA Technical Center, Alcoa Center, PA.

## REFERENCES

1. B. Chalmers: *Principles of Solidification*, John Wiley, New York, NY, 1964.
2. A. Ohno: *Solidification: The Separation Theory and Its Practical Applications*, Springer-Verlag, Berlin, 1987.
3. W. Kurz and D.J. Fisher: *Fundamentals of Solidification*, Trans. Tech. Publications, Switzerland, 1989.
4. S.G.R. Brown and J.A. Spittle: *Mater. Sci. Technol.*, 1989, vol. 5, pp. 362-68.
5. J.D. Hunt: *Mater. Sci. Eng.*, 1984, vol. 65, pp. 75-83.
6. S.C. Flood and J.D. Hunt: *Appl. Sci. Res.*, 1987, vol. 44, pp. 27-42.
7. S.C. Flood and J.D. Hunt: *J. Crystal Growth*, 1987, vol. 82, pp. 552-60.
8. M. Rappaz: *Int. Met. Rev.*, 1989, vol. 34, pp. 93-123.
9. B. Giovanola and W. Kurz: *Metall. Trans. A*, 1990, vol. 21A, pp. 260-63.
10. P. Zhu and R.W. Smith: *Acta Metall. Mater.*, 1992, vol. 40, pp. 3369-79.
11. M. Rappaz and Ch.-A. Gandin: *Acta Metall. Mater.*, 1993, vol. 41, pp. 345-60.
12. R.B. Mahapatra and F. Weinberg: *Metall. Trans. B*, 1987, vol. 18B, pp. 425-32.
13. I. Ziv and F. Weinberg: *Metall. Trans. B*, 1989, vol. 20B, pp. 731-34.
14. F. Weinberg: in *Proc. F. Weinberg Int. Symp. on Solidification Processing*, J.E. Lait and I.V. Samarasekera, eds., Pergamon Press, New York, NY, 1990, pp. 3-11.
15. C.Y. Wang and C. Beckermann: *Metall. Trans. A*, 1993, vol. 24A, pp. 2787-2802.
16. C.Y. Wang and C. Beckermann: *Mater. Sci. Eng. A*, 1993, vol. A171, pp. 199-211.
17. W. Kurz, B. Giovanola, and R. Trivedi: *Acta Metall.*, 1986, vol. 34, pp. 823-30.
18. J. Lipton, M.E. Glicksman, and W. Kurz: *Mater. Sci. Eng.*, 1984, vol. 65, pp. 57-63.
19. D.M. Stefanescu, G. Upadhya, and D. Bandyopadhyay: *Metall. Trans. A*, 1990, vol. 21A, pp. 997-1005.
20. J.D. Hunt: *Solidification and Casting of Metals*, Metals Society, London, 1979.
21. W. Kurz and D.J. Fisher: *Acta Metall.*, 1981, vol. 29, pp. 11-20.
22. H. Jones: *Mater. Sci. Eng.*, 1984, vol. 65, pp. 145-56.
23. M. Rappaz and Ph. Thevoz: *Acta Metall.*, 1987, vol. 35, pp. 1487-97.

24. Ph. Thevoz, J.L. Desbiolles, and M. Rappaz: *Metall. Trans. A*, 1989, vol. 20A, pp. 311-22.
25. S.V. Patankar: *Numerical Heat Transfer and Fluid Flow*, Hemisphere Publishing Corp., New York, NY, 1980.
26. A.A. Tseng, J. Zou, H.P. Wang, and S.R.H. Hoole: *J. Comput. Phys.*, 1992, vol. 102, pp. 1-17.
27. V.R. Voller: *Numer. Heat Transfer*, Part B, 1990, vol. 17, pp. 155-69.
28. T.P. Battle and R.D. Pehlke: *Metall. Trans. B*, 1990, vol. 21B, pp. 357-75.
29. D.R. Poirier: *Metall. Trans. A*, 1988, vol. 19A, pp. 2349-54.
30. M. Gunduz and J.D. Hunt: *Acta Metall.*, 1985, vol. 33, pp. 1651-72.
31. J. Lipton, W. Heinemann, and W. Kurz: *Arch. Eisenhüttenwes.*, 1984, vol. 55, pp. 195-200.
32. S.G.R. Brown and J.A. Spittle: in *Modeling of Casting, Welding and Advanced Solidification Processes V*, M. Rappaz, M.R. Ozgu, and K.W. Mahin, eds., TMS-AIME, Warrendale, PA, 1991, pp. 395-402.
33. V.K. Suri, N. El-Kaddah, and J.T. Berry: *AFS Trans.*, 1991, vol. 99, pp. 187-91.